

ARTICLE OPEN



Multi-objective parametrization of interatomic potentials for large deformation pathways and fracture of two-dimensional materials

Xu Zhang^{1,6}, Hoang Nguyen^{1,6}, Jeffrey T. Paci², Subramanian K. R. S. Sankaranarayanan³, Jose L. Mendoza-Cortes⁴ and Horacio D. Espinosa^{1,5}✉

This investigation presents a generally applicable framework for parameterizing interatomic potentials to accurately capture large deformation pathways. It incorporates a multi-objective genetic algorithm, training and screening property sets, and correlation and principal component analyses. The framework enables iterative definition of properties in the training and screening sets, guided by correlation relationships between properties, aiming to achieve optimal parametrizations for properties of interest. Specifically, the performance of increasingly complex potentials, Buckingham, Stillinger-Weber, Tersoff, and modified reactive empirical bond-order potentials are compared. Using MoSe₂ as a case study, we demonstrate good reproducibility of training/screening properties and superior transferability. For MoSe₂, the best performance is achieved using the Tersoff potential, which is ascribed to its apparent higher flexibility embedded in its functional form. These results should facilitate the selection and parametrization of interatomic potentials for exploring mechanical and phononic properties of a large library of two-dimensional and bulk materials.

npj Computational Materials (2021)7:113; <https://doi.org/10.1038/s41524-021-00573-x>

INTRODUCTION

Molecular dynamics (MD) simulation based on force fields is a powerful tool for studying the temporal behaviors of materials at submicron scales. With continual improvements in hardware and algorithms, MD simulations are becoming increasingly accurate and widely adopted in several frontier problems in materials science and biology¹. While such advances have greatly expanded the capability of MD simulations in size, timescale, and complexity, their predictive powers rely heavily on the accuracy of empirical interatomic potentials in approximating the interactions between atoms. Given the rapid emergence of new two-dimensional (2D) materials^{2,3} that have demonstrated promising electrical, chemical, optical, thermal, and mechanical properties, an increasing demand for accurate interatomic potentials needs to be fulfilled to facilitate mechanistic understandings of their behaviors at scales representative of those used in applications.

Typically, interatomic potentials are formulated for a specific class of materials and are parameterized for a selected list of properties. Consequently, their accuracies on materials beyond the target class or for properties not included in the parametrization need further validation by more accurate methods, i.e., *ab initio* calculations. When those validations are conducted, in general they fail to achieve accurate predictions and reparametrization or new formulations are necessary. For instance, a reactive many-body potential parameterized for molybdenum disulfide⁴ was found to yield artificial stiffening at large strain, and an *ad hoc* parameter-tuning was conducted to correct such behavior⁵. A more systematic interatomic potential parametrization would be indispensable in this case, but becomes a complex and specialized task that requires strong domain expertise and in

most cases deep chemical intuition. One of the complexity of the parametrizing procedure is to reasonably capture nonequilibrium properties, such as vacancy formation energies and uniaxial tension behaviors at the same time. Typical training data (structures, energies, and bond stiffness of atomic clusters or primitive cells^{6–8}) are found insufficient to accurately reflect such properties^{5,9}. Furthermore, there is little guidance beyond chemical intuition for choosing more appropriate training data, thus posing potential limitations on the accuracy and efficiency of the parametrization. Another complication arises due to the fact that interatomic potentials are often parameterized for a finite number of target properties, and some multi-objective optimization schemes may inevitably rely on human interventions. Specifically, a common approach, the weighted-sum method, converts the multi-objective problems into single-objective problems with user-defined, objective-specific weights^{10–12}. However, the choice of *a priori* weights may bias the optimization¹³, thus limiting a holistic evaluation of the performance of interatomic potentials on various properties. This motivated researchers to formulate other optimization approaches, e.g., the Pareto front approach^{14,15}. The last problem of the parametrization is to obtain a set of parameters for a chosen potential form. The selection of a potential form for a new material requires a vast domain knowledge of not only the physics of the material at hand, but also the specific details of such a form. This limitation inevitably hinders the big-picture view of whether interatomic potentials can be parametrized to simulate the behaviors of some special class of materials, e.g., 2D materials, whose atomic structures and properties are distinct from bulk crystals. As a

¹Theoretical and Applied Mechanics Program, Northwestern University, Evanston, IL, USA. ²Department of Chemistry, University of Victoria, Victoria, BC, Canada. ³Center for Nanoscale Materials, Argonne National Laboratory, Lemont, IL, USA. ⁴Department of Chemical Engineering & Materials Science, Michigan State University, East Lansing, MI, USA. ⁵Department of Mechanical Engineering, Northwestern University, Evanston, IL, USA. ⁶These authors contributed equally: Xu Zhang, Hoang Nguyen.

✉email: espinosa@northwestern.edu

result, it prevents a direct comparison of performance between various potentials for the same material.

Despite several successful parametrizations over the past decade^{4,10,16–22}, an in-depth evaluation of the suitability of existing interatomic potentials for the prediction of phase transition and fracture of 2D materials is still lacking. Herein, we propose a robust parametrization method built upon density functional theory (DFT) data sets (considered as ground truth) and the evolutionary multi-objective optimization algorithm, NSGA-III²³. Similar to other genetic algorithms, NSGA-III avoids the dependence on gradient computation, hence it can be applied to any functional form (potential). In addition, this algorithm enables a generation of more widely distributed points on the Pareto front in the criterion space, allowing a more thorough search for an optimum interval. As a result, this algorithm, along with adoption of a machine-learning-inspired protocol, shows good transferability and performance, and offer higher parametrization flexibility. The proposed method is applied to several interatomic potentials of increasing complexity, namely, Buckingham²⁴, Stillinger-Weber (SW)⁷, and Tersoff⁸ for the structural, mechanical, and thermal properties of monolayer 2D materials in both the equilibrium and nonequilibrium regimes (see “Parametrization method” for our classification of properties). The modified reactive empirical bond-order potential for transition metal dichalcogenides (referred to as REBO-TMDC)⁴ is also considered for comparison. As a case study, we perform the parametrization of MoSe₂ and prioritize its mechanical behavior. We use the structure and stability of various surfaces, and thermal properties to examine the interatomic potentials’ transferability. All of the parameterized potentials have better accuracy in nonequilibrium properties when compared with existing MoSe₂ potentials, highlighting the effectiveness of the proposed parametrization method. We further explore the parametrization flexibility of the selected interatomic potentials by conducting correlation and principal component analyses on their prediction errors, which reveals a positive correlation between the complexities of interatomic potentials, their flexibility, and their performances on MoSe₂. Together, these results suggest a robust potential parametrization approach and a quantitative potential selection criterion, which may be generalized for a wide range of materials and materials properties beyond those explored in this study.

RESULTS

Selection of materials and interatomic potentials

Among existing 2D materials, TMDC are one group of materials described by MX₂, where M is a transition metal (Mo, W, etc.) and X is from the oxygen family (S, Se, etc.). Most TMDCs in monolayer form are semiconducting with strong photoluminescence²⁵, thus making them promising candidates for applications, such as transistors²⁶, photodetectors²⁷, supercapacitor electrodes²⁸, and solar cells²⁹. We set out to parameterize interatomic potentials for TMDCs with a focus on failure-related properties, which are critical to the stability and reliability of systems that require frequent mechanical deformation, e.g., flexible electronics. Specifically, we selected monolayer MoSe₂ and its stable phase 2H for which existing interatomic potentials, parameterized primarily for equilibrium properties (structures at equilibrium, phonon dispersion, etc.)^{16,30}, show major deviations in comparison to DFT for nonequilibrium properties, including surface stability and uniaxial stress–strain response. This implies necessities to expand the parametrization to the nonequilibrium regime, defined as states with large perturbations from the equilibrium positions or systems possessing point defects.

We selected interatomic potentials according to their applicability for TMDCs and ability to describe atomic chemical environments. To the best of our knowledge, existing

parametrizations for TMDCs include SW potentials for the mechanical and thermal properties of MoS₂^(10,16,18,20), MoSe₂^(16,31), and WSe₂⁽³¹⁾; a Tersoff potential for the thermal properties of WSe₂²¹; a ReaxFF potential for the mechanical and transitional behaviors of MoS₂^(17,32); and a REBO-TMDC potential for the interfacial and mechanical properties of MoS₂^(4,5). Those interatomic potentials can be segmented into cluster potentials (SW), cluster functionals (Tersoff), and reactive cluster functionals (ReaxFF and REBO-TMDC) with increased levels of complexity and capabilities³³. Specifically, from the simplest pair potentials (e.g., Lennard-Jones potentials), cluster potentials introduce many-body (>2) interactions, cluster functionals incorporate bond-order terms for coordination-dependent bond strength, and reactive cluster functionals enable simulation of chemical reactions. Herein, we chose SW, Tersoff, REBO-TMDC, and also the Buckingham potential²⁴, a simple pair potential widely used for ionic crystals. The formulations of the selected interatomic potentials are detailed in Supplementary Note 4.

Parametrization method

Parametrization of the selected interatomic potentials was performed in an iterative manner. Each iteration consists of three steps, referred to as training, screening, and evaluation (Fig. 1). In the training step, the parameters of the interatomic potentials are optimized with the multi-objective genetic algorithm to minimize the errors for a selected group of properties in comparison to ab initio data. Next, the optimized parameters are screened for the remaining properties with a set of user-specified maximum percentage errors to identify promising candidates. Such a protocol is inspired by machine-learning methods, in which the full data set is separated into training and validation sets to balance underfitting and overfitting³⁴. The evaluation step, including correlation and principal component analyses, is deployed to identify the correlation relationships between properties and redundancy in them. The information is used to (a) guide the selection of training and screening properties for the next iteration, and (b) to quantify parametrization flexibilities of interatomic potentials.

To predict the failure of MoSe₂, we hypothesized that an essential list of materials properties (Fig. 2), in both the equilibrium and nonequilibrium regime, needs to be captured by the interatomic potentials. In the equilibrium regime, we selected the lattice structure and cohesive energy of MoSe₂ at equilibrium, equation of state (near equilibrium), elastic constants (C₁₁ and C₁₂), surface energies (armchair (AC) and zigzag (ZZ) surfaces), and surface stability. For nonequilibrium properties, we selected the following: bond dissociation energy landscapes (along the AC and ZZ directions), vacancy formation energies (seven types), and uniaxial stress–strain curves under elastic instability and soft mode (along the AC and ZZ directions, see Supplementary Note 1 for discussion on elastic instability and soft mode). Moreover, the energy landscape of a 2H–1T phase transition was included to characterize phase changes observed in TMDCs under uniaxial and biaxial strain³⁵, doping³⁶, or vacancy reorganization³². For the Tersoff and REBO-TMDC potential, an additional set of properties for Se systems is needed. Following Chan et al.²¹, we selected the structures and cohesive energies of Se clusters (Se₂, Se₃, Se₆, and Se₈), stability and dissociation of Se₆ and Se₈, and expanded the nonequilibrium regime by including the dissociation energy landscapes for Se₃, Se₆, and Se₈ (see Supplementary Note 3). Ab initio calculations at the DFT level of theory were carried out on all the above properties, which were used as ground truth for parameterizing the interatomic potentials.

The properties are divided into optimization and validation sets. The former is further segmented into training and screening sets, and the optimized parameters are then applied into the validation set after the optimization is finalized. Some training properties

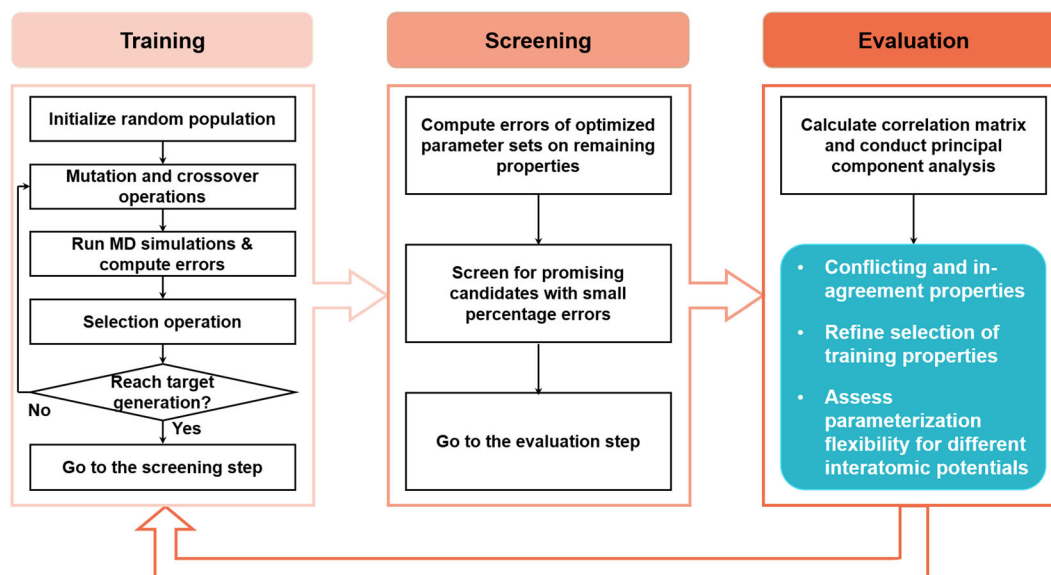


Fig. 1 Schematic of interatomic potential parametrization approach. In the training step, the multi-objective genetic algorithm NSGA-III is used to optimize the parameters of the interatomic potentials for the training properties (Fig. 2). MD simulations are integrated into the genetic algorithm workflow for the evaluation of errors. After reaching a predefined number of generations, the optimization terminates, and the optimized parameters are passed to the screening step for the evaluation of the screening properties (Fig. 2). The training and screening properties together are considered for the selection of promising candidates with percentage errors for all properties within a user-specified threshold. Meanwhile, correlation and principal component analyses are carried out in the evaluation step to reveal the correlation relationships between properties and the performance of interatomic potentials. This information guides the selection of training properties for the next iteration of parametrization.

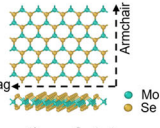
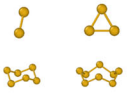
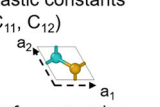
	MoSe ₂		Se (for Tersoff and REBO-TMDC potentials)	
	Equilibrium properties	Non-equilibrium properties	Equilibrium properties	Non-equilibrium properties
Training	<ul style="list-style-type: none"> Lattice structure and cohesive energy  <ul style="list-style-type: none"> Equation of state 	<ul style="list-style-type: none"> Bond dissociation energy landscape (along armchair and zigzag direction) Uniaxial stress-strain curves under elastic instability (armchair and zigzag) 	<ul style="list-style-type: none"> Structures and cohesive energies of Se₂, Se₃, Se₆, and Se₈ clusters 	<ul style="list-style-type: none"> Dissociation energy landscape of Se₃, Se₆, and Se₈
	<ul style="list-style-type: none"> Elastic constants (C₁₁, C₁₂)  <ul style="list-style-type: none"> Surface energies (armchair and zigzag) Stability at 300K 	<ul style="list-style-type: none"> Vacancy formation energies Uniaxial stress-strain curves under soft mode (armchair and zigzag) 2H-1T phase transition energy landscape 	<ul style="list-style-type: none"> Stability of Se₆ at 500K Stability of Se₈ at 393K 	<ul style="list-style-type: none"> Dissociation of Se₆ at 4085K Dissociation of Se₈ at 2200K

Fig. 2 Target properties of monolayer MoSe₂ and Se systems. The properties are segmented with regard to their regime (equilibrium versus nonequilibrium), as well as their purposes for the parametrization (training versus screening). Properties of MoSe₂ are used for all interatomic potentials, while properties of Se are only used for parameterizing single-element interactions of the Tersoff and REBO-TMDC potentials. Atomic illustrations show the structure of MoSe₂ and Se clusters.

imply screening properties and vice versa, although they contain some inherently different information, e.g., the near-equilibrium data points of uniaxial stress–strain curves versus elastic constants, uniaxial stress–strain curves under elastic instability versus curves under soft mode (see Supplementary Note 1). We started an optimizing process by selecting simple properties for training, such as bond dissociation energy landscapes, and more complex properties, e.g., vacancy formation energies, as screening

properties^{17,18}. Another factor that affected this choice is the size and type of calculation needed to be carried out for a given property. For example, a single-point energy calculation would be favored over one that requires MD equilibration, and a system consisting of a primitive unit cell will be prioritized unless a larger system with more atoms would provide more representative data. This criterion accelerates the optimization since the simpler properties often require single-point calculations that are faster

to perform than those that require energy minimization or extra MD steps. These extra steps occasionally suffered from convergence issues due to the emergence of unphysical interatomic potential parameters during the first several steps of optimization. Moreover, properties of the same general attribute, i.e., uniaxial stress–strain curves, were used in both stages with different levels of perturbation. Specifically, stress–strain curves under elastic instability were used as training properties and the curves under soft mode were used as screening properties (see Supplementary Note 1). As such, we selected the following properties as training properties: lattice structure and cohesive energy at equilibrium, equation of state, bond dissociation energy landscapes along both the AC and ZZ directions, and uniaxial stress–strain curves under elastic instability along both the AC and ZZ directions. We note that such a choice is not fixed. Rather, its effect on the parametrization results can be determined from the correlation analysis, as discussed later.

Our training step involves solving a multi-objective optimization problem for which two major approaches prevail: scalarization and vector optimization methods¹³. Scalarization methods convert multi-objective optimization problems into single-objective optimization problems using methods such as weighted-sum, and are predominantly used for parameterizing interatomic potentials. On the other hand, vector optimization methods treat each objective independently and aim at exploring the Pareto optimal solutions—solutions that cannot be further improved without worsening at least one objective. These methods assign equal importance to each objective and allow users to emphasize or exclude certain objectives without biasing the optimization. This is helpful in preventing solutions from being swamped out, but may be a limitation if relative importance between objectives is known. We overcame this limitation in the screening step by assigning a lower objective-specific percentage error (discussed later), if one wants to focus on a specific property. Among various vector optimization methods, we adopted a multi-objective genetic algorithm named NSGA-III²³. As a genetic algorithm, it conducts a global optimization through an iterative process that loosely mimics Darwin's theory of natural selection, i.e., via mutation, crossover, and selection operations on a population of individuals. Moreover, the algorithm incorporates a nondominated sorting procedure and a niche-preservation operator to identify nondominated individuals that are well-spread in the criterion space. As a result, this specific algorithm shows superiority by sampling more widely distributed points on the Pareto front. To the best of our knowledge, we report the first application of NSGA-III for parameterizing interatomic potentials. In most optimization problems with three to ten objectives, it outperforms its predecessor, NSGA-II³⁷, which has been the predominant algorithm applied in similar problems^{14,15}. Moreover, we found that it is more efficient in overcoming local minimum states during the optimization in comparison to a hierarchical genetic algorithm optimization framework²¹ (see Supplementary Note 2).

As shown in Fig. 1, the optimization starts from an initial population of individuals (i.e., sets of parameters for a given interatomic potential) that are randomly generated within a predefined range according to potential-specific requirements (see Supplementary Note 4). In each generation, mutation and crossover operations are first conducted on the current population according to specified probabilities. The parameters after mutation and crossover are not allowed to exceed the predefined initialization range. The value to be minimized for each objective during the optimization, i.e., the fitness value, is defined as follows:

$$f_i(\mathbf{x}) = \sum_{j=1}^K w_i^j \left(v_i^j(\mathbf{x}) - \hat{v}_i^j \right)^2; i = 1, \dots, M_t \quad (1)$$

where \mathbf{x} represents an individual whose dimension equals the number of parameters to be optimized for a given interatomic

potential, $v_i^j(\mathbf{x})$ denotes predictions from interatomic potentials with parameter set \mathbf{x} for objective i , \hat{v}_i^j represents ab initio results for objective i , superscript j represents the j th point for objective i , and w_i^j is the corresponding weight for the j th point. The weight is used to emphasize certain regions of the training data, e.g., the elastic regime of the stress–strain curves. The values of the weights are provided in Supplementary Note 10, and are found to have an insignificant effect on parametrization results. The point-wise errors are squared, scaled, and summed over all points for objective i . Thus, the fitness value is the squared error for objectives with $K = 1$ (e.g., elastic constant C_{11} etc.), and is the sum of (weighted) squared errors for objectives with $K > 1$ (e.g., stress–strain curves). For each parameter set \mathbf{x} , there are M_t fitness values corresponding to the M_t training objectives (properties). Individuals of the current generation are ranked based on whether they are dominated by other individuals. An individual \mathbf{x} is nondominated if and only if there does not exist another individual \mathbf{x}^* in the current population such that $f_i(\mathbf{x}^*) \leq f_i(\mathbf{x})$ for any i with at least one $f_i(\mathbf{x}^*) < f_i(\mathbf{x})$. All nondominated individuals (Pareto optimal solutions) are ranked lowest and are selected first, followed by individuals that are only dominated by those Pareto optimal solutions and so on. The selected individuals are passed to the next generation, where the same protocol repeats until the predefined total number of generations is reached. For each interatomic potential, multiple optimizations are carried out concurrently with different random seeds to explore a large parameter space and various optimization paths.

Prior to the screening step, the optimized individuals from multiple optimizations are gathered, and the fitness values for the remaining properties (screening properties in Fig. 2) are calculated following Eq. (1). Those values are combined with the fitness values of the training properties to form a matrix of dimension $N \times M$, where N is the total number of optimized individuals and M is the total number of properties. This matrix is then screened with the criterion defined as follows:

$$f_i(\mathbf{x}) \leq \sum_{j=1}^K w_i^j \left(p_i \hat{v}_i^j \right)^2; i = 1, \dots, M \quad (2)$$

where $f_i(\mathbf{x})$, w_i^j , and \hat{v}_i^j follow the same definitions as in Eq. (1), and p_i is an objective-specific percentage value. The criterion defines a maximum percentage error for objectives with one data point ($K = 1$), and resembles the sum of squared percentage error (SSPE) for objectives with multiple data points. Indeed, this criterion and the SSPE measurement agree well in magnitude and variation according to a sampling test on a harmonic function (see Supplementary Note 6). The parameters p_i reflect the relative importance of each objective and provide a desirable level of flexibility for the parametrization without biasing the optimization, which is a major advantage over the prevalent weighted-sum method. The parameter sets that pass the screening step are deemed promising candidates.

Our approach is unique in several respects. In our implementation of screening sets, we used explicit criteria for selecting fittest interatomic potential parameters and evaluating the parametrization flexibility. This emerges when we evaluate the effect of one criterion on the validation properties or the entire set of properties. This approach is different to most, if not all, parametrization of empirical interatomic potentials in which the validation sets are used for examining the presumptive transferability instead of guiding the optimization. For instance, the validation test for a recently developed CHARMM force field³⁸ is conducted on chemically similar species with respect to the optimization sets. Such a validation should and indeed does reveal good transferability as it follows the underlying assumptions of the CHARMM General Force Field³⁹. By contrast, several interatomic potentials for MoSe₂, as reported in the literature, have poor transferability (see the next section). In the present approach,

Table 1. Comparison of the parameterized interatomic potentials with ab initio results.

	Ab initio	Buckingham	SW	Tersoff	SW (Kandemir et al. ¹⁶)	SNAP (Gu and Zhao ³⁰)
E_{coh} (eV)	−4.77	−3.33	−4.35	−5.10	−4.59	−2.11
$d_{\text{Mo-Se}}$ (Å)	2.57	2.47	2.48	2.52	2.54	2.53
$d_{\text{Se-Se}}$ (Å)	3.39	3.08	3.10	3.25	3.29	3.26
C_{11} (GPa)	129.34	145.66	124.59	129.29	149.96	138.52
C_{12} (GPa)	35.36	62.82	13.66	22.78	57.28	28.77
Γ_{ZZ} (eV Å ^{−1})	0.72	0.67	0.43	0.39	1.17	— ^a
Γ_{AC} (eV Å ^{−1})	0.77	0.74	0.64	0.42	1.35	—
E_{Mo} (eV)	6.51	2.85	7.25	5.59	0.60	—
E_{Mo2F} (eV)	11.69	5.70	14.53	10.61	1.20	—
E_{Mo2C} (eV)	10.44	5.39	14.10	10.55	0.17	—
E_{Se} (eV)	3.30	0.62	0.57	2.14	6.93	4.12
E_{Se2} (eV)	6.23	3.92	4.20	3.98	12.52	7.24
E_{MoSe3} (eV)	10.94	1.66	4.76	8.51	16.70	—
E_{MoSe6} (eV)	20.27	6.64	8.78	10.79	15.71	—
RMSD at 300 K (Å)	—	0.25	0.25	0.24	0.15	0.25

Two existing SW¹⁶ and SNAP³⁰ potentials for monolayer MoSe₂ are also included. The comparison includes predictions of cohesive energy per atom, E_{coh} , equilibrium distance between Mo–Se and Se–Se atoms (Se atoms above and below the Mo layer), elastic constants C_{11} and C_{12} , armchair and zigzag surface energies Γ_{AC} and Γ_{ZZ} , vacancy formation energies of Mo monovacancy E_{Mo} , non-adjacent Mo divacancies E_{Mo2F} , adjacent Mo divacancies E_{Mo2C} , Se monovacancy E_{Se} , Se divacancies (one above and one below the Mo layer) E_{Se2} , one Mo and three adjacent Se vacancies (in the same Se atomic layer) E_{MoSe3} , one Mo and six adjacent Se vacancies E_{MoSe6} , and root mean square displacements (RMSD) at 300 K.

^aA dash denotes that the system with surface or vacancy undergoes significant structural changes, and cannot be equilibrated with the SNAP potential.

the improvement on transferability can be done by redefining allowable errors for the screening sets (and training sets) that have more impact on a desired validation property (e.g., phonon dispersion and thermal conductivity). Thanks to this protocol, we were able to ascertain transferability and infer directions for balancing parametrization tradeoffs of specific properties. Lastly, we introduced correlation and principal component statistical analyses to ascertain correlation relationship between properties and infer parametrization flexibilities of interatomic potentials, both of which remain unexplored in the literature. We note that the statistical information closes the parametrization loop by guiding the selection of training and screening properties for the next iteration, as further elaborated in subsequent sections.

Parametrization results

Table 1 and Fig. 3 summarize the predictions of the parameterized interatomic potentials in comparison to ab initio calculations, as well as existing SW¹⁶ and SNAP³⁰ potentials for monolayer MoSe₂. In selecting the parameter sets for each interatomic potential with Eq. (2), we emphasize the accuracy of uniaxial stress–strain curves (under soft mode), while maintaining other properties to be at least within 90% error. The parameterized potentials are listed in Supplementary Note 5. Not surprisingly, since the SW potential parameterized by Kandemir et al. and the SNAP potential parameterized by Gu and Zhao are primarily trained for equilibrium properties, including structures and thermal transport, they show limited accuracy for the nonequilibrium properties studied herein: vacancy formation energies (Table 1) deviate from ab initio results (the surface and vacancies structures cannot be equilibrated with the SNAP potential); bond dissociation energy landscapes along the AC (Fig. 3a) and ZZ (Fig. 3b) directions deviate from ab initio curves at strain > 0.1; uniaxial stress–strain curves along both the AC (Fig. 3e) and ZZ (Fig. 3f) directions deviate significantly from ab initio results at strains larger than 0.05. In comparison, the parameterized interatomic potentials here reported yield predictions that are vastly more accurate for those properties due to the augmented ab initio training data in the

nonequilibrium regime and an explicit screening step that further defines maximum allowable errors.

Figure 3d shows the phase transition energy landscape identified by climbing image nudged elastic band simulations⁴⁰ (see Supplementary Video 1 for the movie of this simulation). Under the screening criteria, which prioritize stress–strain responses, all the parameterized interatomic potentials incorrectly predict the 1T phase to be the minimum energy state. For the Tersoff potential, an individual with the correct relative energy between the 2H and 1T phase have less accuracy on other properties (see Supplementary Note 7). The results suggest an important limitation of the Tersoff potential, which is the capturing of the phase transition energy landscape. This finding is confirmed by the correlation analysis discussed in the next section.

Notably, the Tersoff potential has the overall best performance among the selected interatomic potentials. It provides a smooth uniaxial tension curve closely matching the ab initio results, whereas the Buckingham and SW potentials predict an artificial 2H–1T phase transition during uniaxial tension at ~0.2 strain, manifested as kinks in Fig. 3e, f. This data seems to advocate a positive correlation between the complexity of the interatomic potential and its overall accuracy for monolayer MoSe₂. Such observation is further corroborated by the correlation analysis, as described in the next section. We note the importance of direct force fitting (i.e., stress–strain curves as training data) for the Tersoff potential to achieve good accuracy for uniaxial tension response. Similarly, forces and other higher order derivatives of energies were found critical for accurate predictions of phonon dispersion and thermal transport in crystalline Si and Ge¹¹. Thus, inclusion of force fitting during parametrization should result in better transferability of the interatomic potentials.

Correlation and principal component analyses

As part of the screening step, a matrix of dimension $N \times M$ is constructed where each of the N rows contains the fitness values, Eq. (2), of all the M properties. Treating each row as a sample point

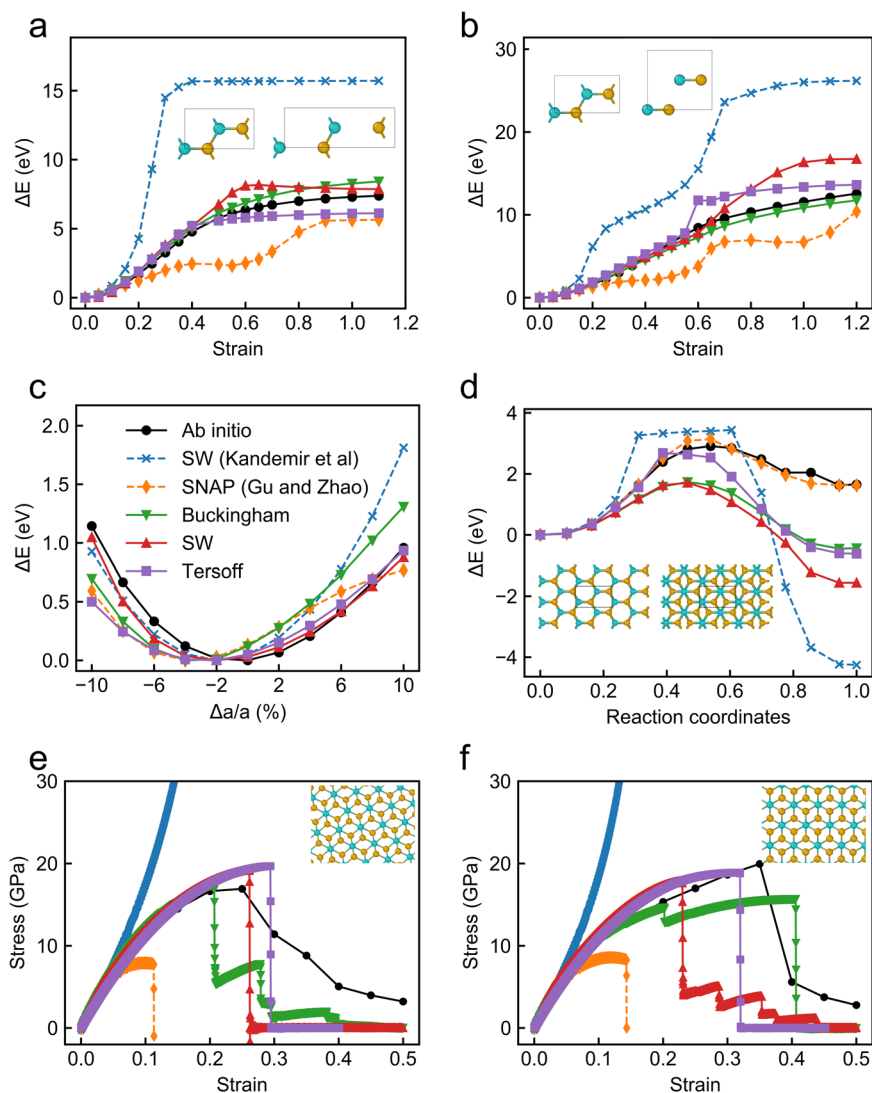


Fig. 3 Prediction results of the parameterized interatomic potentials in comparison to *ab initio* results, as well as the existing SW¹⁶ and SNAP potentials³⁰. **a, b** Bond dissociation energy landscape along the armchair (**a**) and zigzag (**b**) directions. Two snapshots along the landscape are shown and correspond to strain of 0 and 0.6, respectively. **c** Equation of state. **d** 2H-1T phase transition energy landscape. The two snapshots from left to right correspond to reaction coordinates of 0 and 1, respectively (see Supplementary Video 1 for the movie of this simulation). **e, f** Uniaxial stress-strain curve at 1 K in comparison to *ab initio* curves under soft mode (see Supplementary Note 1) along the armchair (**e**) and zigzag (**f**) directions. The snapshots in **e** and **f** show the formation of the 1T phase during uniaxial tension for the Buckingham potential, which is also predicted by the SW potential during uniaxial tension along the zigzag direction. Legends of **a, b, d–f** are identical to that in **c**, and are omitted for clarity. In the atom snapshots, Mo atoms are colored cyan, and Se atoms are colored orange.

in the M -dimensional design space enables a quantitative assessment of the relations between the M properties through statistical analysis. From the $N \times M$ matrix, we construct an $M \times M$ correlation matrix where each element R_{ij} is the Pearson correlation coefficient between property i and property j . A graphical representation of those coefficients for the Tersoff potential is shown in Fig. 4. The correlation coefficients in Fig. 4 correspond to individuals with percentage errors <100% for all properties. Such setting aims at exploring regions in the criterion space where promising candidates are selected. R_{ij} ranges from -1 to 1 , denoting strongly negative and positive correlations, respectively. In the context of our problem, a positive R_{ij} between property i and j indicates simultaneous increase or decrease of their prediction errors, and hence nonconflicting relations between the two properties. In comparison, a negative R_{ij} suggests a conflicting relationship between property i and j : the errors for property i cannot be minimized without compromising the accuracy of property j .

As shown in Fig. 4, the Tersoff potential (the bottom triangle) possesses several pairs of properties that are strongly positively correlated. Conforming to chemical intuition, properties of similar nature have strong positive correlations, e.g., bond dissociation energies along the AC and ZZ directions ($R = 0.7$), AC and ZZ surface energies ($R = 0.9$), and vacancy formation energies of Mo and Mo₂F ($R = 1$). Similar relations were identified for the Buckingham and SW potential (see Supplementary Note 8). The correlation matrix also reveals conflicting properties that cannot be directly deduced from chemical intuition. Specifically, the phase transition energy landscape is conflicting to almost all properties. This agrees with our observation of accuracy degradation of most properties when the phase transition energy landscape is prioritized (see Supplementary Note 7). Thus, the correlation matrix offers a direct gauge of the accuracy (and hence the parameters) of the parameterized interatomic potential on all properties should the relative importance between properties be different.

To assess the parametrization flexibility of any interatomic potential, we propose evaluating a quantity F defined as

$$F = \frac{\sum_{i < j} R_{ij}}{M}; i, j = 1, 2, \dots, M \quad (3)$$

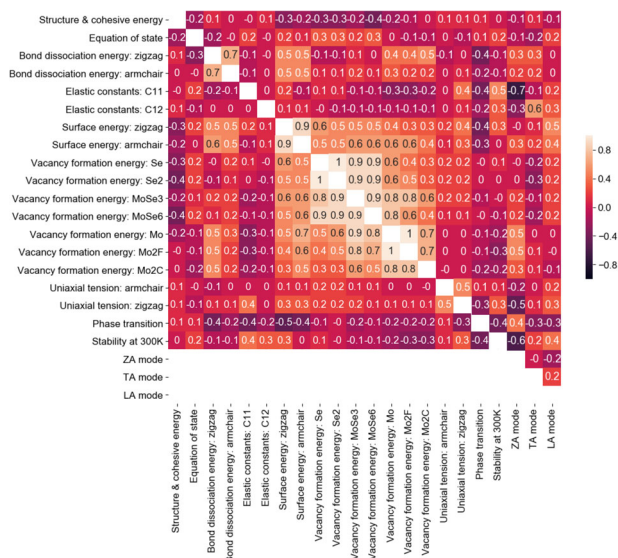


Fig. 4 Correlation matrix of the Tersoff potential. The Pearson correlation coefficient for the corresponding pair of properties, ranging from -1 to 1 , is shown in each cell. When calculating the correlation coefficients, individuals with percentage errors $> 100\%$ for any property were excluded to explore the region in the criterion space, where promising candidates are selected. Two correlation matrices are shown; the bottom corresponds to the as-optimized Tersoff potential and the top corresponds to the same population with additional screening on the three acoustic phonon modes, ZA, LA, and TA. Since each correlation matrix is symmetric, only half of the correlation matrix is shown and the diagonal components (always equal to 1) are removed for clarity. For visualization purposes, all correlation coefficients are rounded to a decimal. Thus, a value of “ -0 ” means the true correlation coefficient is within $[-0.05, 0]$. The cells are colored according to their correlation coefficients. Uniaxial tension items herein refer to curves under soft mode (see Supplementary Note 1).

For an ideal interatomic potential approaching an ab initio level of accuracy, there should exist a region in the criterion space, where the prediction errors of all properties have strong positive correlations, and thus can be minimized simultaneously, which allows a large level of flexibility for parametrization. For the ideal interatomic potential, $F_{\text{ideal}} = (M - 1)/2$. We sampled five regions in the criterion space near 100% percentage errors ($p_i = 80\text{--}120\%$) with enough individuals (>30) in each region. F_{Tersoff} , F_{SW} , and $F_{\text{Buckingham}}$ were found to be 1.44 ± 0.12 , 0.71 ± 0.25 , and 0.77 ± 0.12 , respectively. Notably, the Tersoff potential has the highest flexibility, consistent with our observation that the parameterized Tersoff potential predicts the most accurate uniaxial stress–strain curves.

To further explore the intrinsic relationships between properties, we conducted principal component analysis on the correlation matrix. It was originally proposed to identify redundant objectives during multi-objective optimizations⁴¹, and is used herein to find redundant properties, i.e., properties that can be automatically captured if essential properties are captured with either the training or screening step. The protocol is detailed in Supplementary Note 9. The analysis reveals that all the training data are nonredundant for all the interatomic potentials, thus indicating optimized training properties. Furthermore, it shows that the formation energies of certain vacancies are redundant with respect to others (see Supplementary Note 9), in agreement with chemical intuition.

Validation and transferability of parameterized potentials

We evaluated the validity and transferability of the optimized Tersoff potential on the edge stability and thermal properties of monolayer MoSe₂, which are relevant for applications in nanoelectronics^{16,30} and catalysis⁴², but are not parameterized within the scope of this study. This can also be referred as the “test” data set in other machine learning frameworks³⁴. Figure 5 shows ab initio molecular dynamics (AIMD) and Tersoff predictions on the stability of various edge configurations at 300 K and elevated temperatures. Those configurations correspond to the Mo-Klein, Mo-ZZ, Se-ZZ, and the AC edge, which were identified by scanning transmission electron microscopy (Fig. 5) in nanoporous MoS₂ films grown with molecular beam epitaxy under high Mo flux⁴². The Tersoff potential shows a decent level of transferability owing to its higher flexibility in its functional form: it

Edge type	Mo-Klein		Mo-zigzag		Se-zigzag		Armchair
Atomic configuration							
Temperature	300 K	650 K	300 K	650 K	300 K	750 K	300 K
AIMD	stable		stable		stable		stable
Tersoff	stable		stable		stable		stable
Tersoff-ZTL	stable		stable		stable		stable

stable unstable

Fig. 5 Transferability test for the parametrized potentials (Tersoff and Tersoff-ZTL) on edge stability of monolayer MoSe₂. The edges were observed in nanoporous MoS₂ films grown with molecular beam epitaxy under high Mo flux⁴². Scanning transmission electron microscopy images of the corresponding edge structures for MoS₂ were retrieved from Zhao et al.⁴² and are shown herein. Red dashed lines highlight the Mo atomic layers, and the scale bars represent 0.5 nm. The same edge configuration was equilibrated with ab initio MD (AIMD; for 1 ps) and MD (500 ps) at the specified temperature. An “unstable” configuration is defined as a configuration that undergoes breakage and reformation of chemical bonds during equilibration (see Supplementary Videos 2–5 for the movies of those simulations). We note a longer simulation time for MD to reveal the unstable edge configurations due to limitations of interatomic potentials to reflect electronic interactions embedded in the AIMD simulations. In the atomic snapshots, Mo atoms are colored cyan, and Se atoms are colored orange. The Tersoff-ZTL corresponds to the parameterized potential with the training data of “Tersoff” plus the three acoustic phonon modes, i.e., ZA, LA, and TA. Reprinted (adapted) with permission from Zhao et al.⁴² Copyright (2018) American Chemical Society.

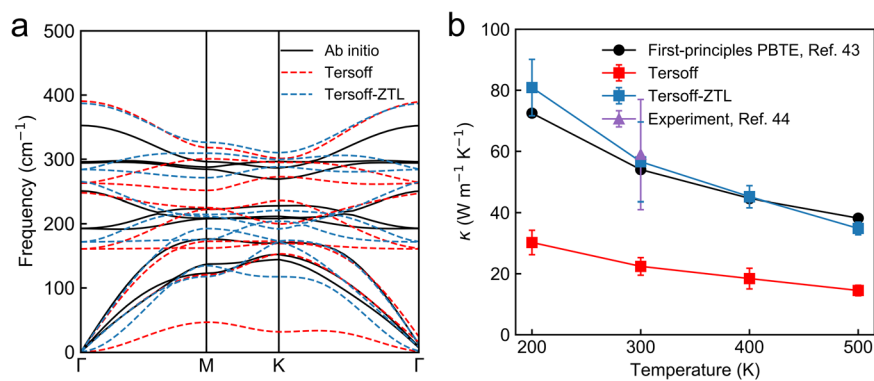


Fig. 6 Transferability test for the parameterized Tersoff potentials (Tersoff and Tersoff-ZTL) on thermal properties of monolayer MoSe₂. **a** Phonon dispersion predicted by the Tersoff potential in comparison to ab initio results. **b** Thermal conductivity predicted by the Tersoff potential in comparison to first principle calculations by solving the Peierls-Boltzmann transport equation (PBTE)⁴³, as well as experimental measurements on suspended monolayer MoSe₂ using optothermal Raman techniques⁴⁴. The Tersoff-ZTL corresponds to the parameterized potential with the training data of “Tersoff” plus the three acoustic phonon modes, i.e., ZA, LA, and TA.

reproduces AIMD predictions for all the edges at 300^oK, for the Mo-Klein and Se-ZZ edges at elevated temperatures (650 and 750^oK, respectively), but tends to overstabilize the Mo-ZZ edges at 650^oK (see Supplementary Videos 2–5 for the movies of those simulations). Figure 6a shows the phonon dispersions predicted by the parameterized Tersoff potential in comparison to the ab initio results. The Tersoff potential predicts no negative frequency and correct Γ point for acoustic bands albeit lower frequencies for the out-of-plane (ZA) mode and a smaller phonon band gap. Such inconsistency results in lower in-plane thermal conductivity in comparison to first-principles calculations⁴³ and experimental measurements on a suspended monolayer MoSe₂ membrane⁴⁴, as shown in Fig. 6b. However, we note that the excellent accuracy of the longitudinal (LA) and in-plane transversal acoustic band (TA) was captured by the Tersoff potential, due to the inclusion of force fitting in training, i.e., uniaxial stress–strain curves along two directions.

We next discuss how the correlation and principal component analyses are employed to close the parametrization loop and improve the accuracy of phonon dispersion. We screened the optimized Tersoff population on the three acoustic phonon modes, and conducted a correlation analysis. The correlation matrix (Fig. 4, top triangle) shows that the ZA mode is more conflicting to other properties in comparison to the TA and LA modes, i.e., for C_{11} , uniaxial stress–strain curves along the ZZ direction, and stability at 300^oK. Such results suggest that adding the ZA mode into the training data will increase the accuracy of ZA mode at the expense of decreased accuracy on the aforementioned properties. However, the worsening effect may be mitigated by including the other two modes that possess relatively positive correlation relationships. We carried out two iterations, one with the addition of the ZA mode and the other with the addition of all three modes to the training data set. The results support the above statement (see Supplementary Note 11). Specifically, the iteration with all three modes, referred as Tersoff-ZTL, resulted in a more accurate ZA mode (Fig. 6a) and thermal conductivity (Fig. 6b) with minimum deterioration of other properties (Supplementary Fig. 9 and Fig. 5). We note that the bending rigidity of 2D materials is directly related to the ZA mode⁴⁵. Thus, the Tersoff-ZTL should possess improved accuracy on bending rigidity.

DISCUSSION

We propose a robust approach of parameterizing interatomic potentials. It incorporates the multi-objective genetic algorithm NSGA-III, a machine-learning-inspired protocol, and a correlation

and principal component analyses framework. Using monolayer MoSe₂ as a testbed, we demonstrate the effectiveness of the proposed approach in capturing properties of monolayer MoSe₂ in both the equilibrium and nonequilibrium regimes. Compared with existing parametrization methods, our approach incorporates a more efficient optimization algorithm, provides more flexibility for balancing the tradeoff and priority of specific properties without biasing the optimization, and shows good transferability for various interatomic potentials with different levels of complexity. In all cases, the method is straightforward to implement, given the appropriate computer codes. Moreover, this approach enables the exploration of the intrinsic relationships between properties through correlation and principal component analyses, which is absent in other parametrization frameworks, such as GARField⁴⁶ and Paramfit⁴⁷. With the correlation matrix, one can (a) evaluate the feasibility of improving the parametrization of a given potential; (b) assess the parametrization flexibility of a given potential with the value of F . At this stage, the analyses are used to close the parametrization loop through selections made by the user. An automated workflow could be developed by adopting other machine learning algorithms, such as logistic regression and decision trees on a cross-validating set, which would further minimize human intervention³⁴. Such approaches are left to future studies.

In the approach here presented, the choice of interatomic potentials and parametrization parameters constitute an iterative process. One should start by using computationally inexpensive properties (see the “Parametrization method” section) for training, to cover a wider range of configurations and achieve better optimization efficiency. The correlation and principal component analyses are then employed to guide the selection of training and screening properties for the next iteration, e.g., exclude redundant properties from the training set or include properties into the training set after evaluating the effect on other properties. We note that simple expansion of the data base, without considering their correlation with other properties of interest, is not a suitable approach.

We identified intrinsic conflicting relationships between certain properties for the parameterized interatomic potentials and attributed such behaviors to the limitations of the functional forms. To examine if more sophisticated functional forms can alleviate this issue, we parameterized a modified reactive empirical bond-order potential for TMDCs (referred to as REBO-TMDC)⁴, using the same training data as Tersoff-ZTL. In comparison to Tersoff-ZTL, the REBO-TMDC shows improved accuracy on phase transition, but decreased accuracy on several other properties (see Supplementary Note 12). This suggests that

the intrinsic conflicting roles of properties are always present and that more sophisticated interatomic potentials do not necessarily translate into better accuracy across all properties. Rather, as can be seen from the example of Tersoff and Tersoff-ZTL, attention needs to be paid as to how properties correlate for each functional form (potential).

We leave the parametrization of more complex functional forms, with a larger number of parameters, e.g., ReaxFF⁴⁸, for future work. Nevertheless, when equilibrium properties are the primary interest of parametrization, simpler interatomic potentials are worth exploring due to the ease of parametrization and better computational efficiency. Indeed, common interatomic potentials were found to be overdesigned for the purpose of exclusively modeling equilibrium properties, including phonon dispersion and thermal transport in crystalline Si and Ge¹¹, thus suggesting sufficient flexibilities for parametrization. In either circumstance, our approach offers a framework for future studies aiming at expanding the capability of empirical interatomic potentials for quantifying unconventional chemical and physical phenomena in emerging new materials.

We highlight the better performance of the NSGA-III algorithm over several existing multi-objective global optimization algorithms. We also note that other multi-objective global optimization algorithms, e.g., MOES⁴⁹ and GARField⁴⁶, have been developed for parameterizing ReaxFF for molecular crystals and SiC. Future work should perform comparison among existing approaches. Furthermore, for TMDCs, the transferability test can be expanded to other DFT calculations and in situ transmission electron microscopy observations, including vacancy induced phase transition³², formation of inversion domains⁵⁰, atomic morphologies of the crack tip⁵, etc., which we leave for future exploration.

METHODS

Ab initio calculations

The training data for the optimization were created by ab initio calculations. These simulations were carried out using the density functional approach via SIESTA 4.0.2 software⁵¹. We applied the non-spin-polarized generalized gradient approximation in the Perdew-Burke-Ernzerhof (PBE) form⁵² together with the split polarized valence double-zeta (DZP) basis set⁵³. For the molybdenum and selenium atoms, nonrelativistic norm-conserving Troullier-Martins pseudopotentials⁵⁴ were utilized. The energy shift and mesh cutoff were selected to be 250 eV and 300 Ry (~4081 eV), respectively, at which energy convergence was attained. Geometry optimization was conducted without any symmetry constraints, until the forces acting on the atoms became <0.01 eV Å⁻¹. The interaction between monolayers (or molecules) were prevented by a 40 Å vacuum layer. A monolayer thickness of 7.726 Å was used to calculate per-area quantities (e.g., monolayer stresses)⁵⁵. To achieve accurate electronic structure calculations, we allowed a 15 Å cutoff for the set of *k*-points in the first Brillouin zone. The resultant *k*-grids were chosen in an optimal way, according to the method of Moreno and Soler (which utilized an effective super cell close to spherical shape, thus minimizing the number of *k*-points for a given precision)⁵⁶. The self-consistent and the conjugate gradient minimization schemes were employed for the electronic structure calculation and for the geometry optimization, respectively. The cohesive energy of a compound was computed from

$$E_{\text{coh}} = E_{\text{pristine}} - n_{\text{Mo}}E_{\text{Mo}} - n_{\text{Se}}E_{\text{Se}} \quad (4)$$

where E_{pristine} is the energy of the compound, E_{Mo} and E_{Se} are the energies of an isolated Mo and Se atom, and n_{Mo} and n_{Se} are the numbers of corresponding atoms in the compound. The elastic constants were extracted from uniaxial stress-strain curves in the small-deformation regime. A fitting procedure reported by Cooper et al.⁵⁷ was used to extract the polynomial of the finite-deformation Green tensor of different orders, and the second-order terms were used in the screening process. Vacancy formation energies were calculated with the following equation:

$$E_{\text{f}} = E_{\text{defected}} + n_{\text{Mo}}\mu_{\text{Mo}} + n_{\text{Se}}\mu_{\text{Se}} - E_{\text{pristine}} \quad (5)$$

where E_{defected} is the energy of the defected system, E_{pristine} is the energy

of the pristine system, n_{Mo} and n_{Se} are the number of missing Mo and Se atoms in the vacancy, and μ_{Mo} and μ_{Se} are chemical potentials for Mo in its stable BCC structure and Se in Se₈ rings, respectively.

Phonon dispersion calculation

In order to obtain the phonon dispersion curves and densities of states, the theory of lattice dynamics on a Born-Oppenheimer surface was applied. Assuming that atomic displacements are in the form of plane-wave functions with different wave numbers, lattice vibration turns into an eigenvalue problem. Siesta⁵¹ offers utility functions (e.g., *vibra* and *fbuild*) that displace each atom in the monolayer and measure the reaction of other atoms to form the stiffness matrix. The wave dispersion along the path connecting symmetry points of the hexagonal lattice Γ -M-K- Γ in the first Brillouin zone for MoSe₂ monolayers were investigated. These points are located at (0,0,0), (0.5,0,0), and (0.333,0.333,0) in reciprocal space. These symmetry directions stem from the hexagonal lattice 2H MoSe₂, similar to graphene. To sample the dispersion within the first Brillouin zone, a super cell of 4 × 4 × 1 repetitive unit cells was utilized to include all possible attenuations of the real-space force constants within it. To avoid interactions between monolayers, a vacuum layer of 40 Å was set.

Molecular dynamics simulations

MD simulations were conducted with LAMMPS⁵⁸ (3Mar20, serial version for optimization and mpi version for simulating larger systems). To compare MD simulations with ab initio calculations, we used the same atomic systems for most objectives except for the lattice structures and cohesive energies, in which we enlarged the size of the system for better sampling. For energy landscapes (equation of states, bond dissociation, phase transition, and dissociation of Se clusters), single-point calculations were performed on the equilibrated structures from ab initio calculations without energy minimization. For the remaining objectives, an energy minimization step was carried out on the input structures with the conjugate gradient algorithm (energy tolerance 0 eV, force tolerance 10⁻¹⁰ eV Å⁻¹) before calculating the energies. For simulations with MD steps, a time step of 1 fs was used. Phonon dispersion calculations were performed with phonopy (2.4.1.post5)⁵⁹. Thermal conductivity was calculated using the equilibrium Green-Kubo formalism^{60,61}. A monolayer MoSe₂ flake of 2.3 by 2.3 nm was first equilibrated with an NVT ensemble for 0.1 ns, followed by an NVE step of 1 ns during which the ensemble average of the autocorrelation of the heat flux was measured for calculating the thermal conductivity. We computed in-plane thermal conductivities as the average over conductivities along the AC and ZZ direction. The thermal conductivity at a given temperature was further averaged over 6 replicas with different initial random velocities. Atomic visualizations were created with OVITO⁶².

Nudged elastic band simulations

Climbing image nudged elastic band simulations were carried out with LAMMPS⁴⁰. Fourteen replicas including the initial and final configurations were used. The energy and force cutoff for energy minimization were selected to be 0.1 eV and 0.01 eV Å⁻¹. The spring constant for the nudging force was set as 1 eV Å⁻¹. The minimum energy path was found using the Tersoff potential and was adopted by ab initio simulations and other interatomic potentials.

Optimization parameters and system setup

The population size was set to be 156 for the genetic algorithm optimizations following Deb and Jain²³. Each optimization was conducted for 500 generations with which the optimization converged. We submitted 20 runs concurrently with different random seeds. We used a simulated binary crossover operator with a crossover probability of 1 and a crowding degree, η of 30. For mutation operations, we used polynomial mutation with a mutation probability of 1 and a η value of 20. We stored and output statistics of the entire population for every certain number of generations to monitor the optimization progress. After all runs finished, we combined the optimized parameters from all runs for the subsequent screening process. The optimization environment was set up with Python (3.7.7) and the genetic algorithm optimization was based on the DEAP framework (1.3.0)⁶³. Parameter initialization, genetic algorithm operations, and calculations of statistics were conducted with DEAP. When the evaluation for an individual was needed, the code initiated a LAMMPS calculation via a system-level call, and read the output from LAMMPS log files.

Parallel programming was enabled by SCOOP (0.7.1.1)⁶⁴ to offer accelerated performance on supercomputer clusters. The optimization times scaled with the complexity of the interatomic potentials and were in the range of several hours to several days.

DATA AVAILABILITY

The parameterized interatomic potentials, as well as the corresponding potential files, are documented and included in the Supplementary Information.

CODE AVAILABILITY

The codes for genetic algorithm optimization and correlation and principal component analyses are available from the corresponding author upon request.

Received: 3 November 2020; Accepted: 16 June 2021;

Published online: 21 July 2021

REFERENCES

- Hollingsworth, S. A. & Dror, R. O. Molecular dynamics simulation for all. *Neuron* **99**, 1129–1143 (2018).
- Butler, S. Z. et al. Progress, challenges, and opportunities in two-dimensional materials beyond graphene. *ACS Nano* **7**, 2898–2926 (2013).
- Geim, A. K. & Novoselov, K. S. In *Nanoscience and Technology: A Collection of Reviews from Nature Journals*, 11–19 (World Scientific, 2010).
- Liang, T., Phillpot, S. R. & Sinnott, S. B. Parameterization of a reactive many-body potential for Mo–S systems. *Phys. Rev. B* **79**, 245110 (2009).
- Wang, S. et al. Atomically sharp crack tips in monolayer MoS₂ and their enhanced toughness by vacancy defects. *ACS Nano* **10**, 9831–9839 (2016).
- Brenner, D. W. et al. A second-generation reactive empirical bond order (REBO) potential energy expression for hydrocarbons. *J. Phys. Condens. Matter* **14**, 783 (2002).
- Stillinger, F. H. & Weber, T. A. Computer simulation of local order in condensed phases of silicon. *Phys. Rev. B* **31**, 5262 (1985).
- Tersoff, J. New empirical approach for the structure and energy of covalent systems. *Phys. Rev. B* **37**, 6991 (1988).
- Belytschko, T., Xiao, S., Schatz, G. C. & Ruoff, R. Atomistic simulations of nanotube fracture. *Phys. Rev. B* **65**, 235430 (2002).
- Wen, M. et al. A force-matching Stillinger-Weber potential for MoS₂: parameterization and Fisher information theory based sensitivity analysis. *J. Appl. Phys.* **122**, 244301 (2017).
- Rohskopf, A., Seyf, H. R., Gordiz, K., Tadano, T. & Henry, A. Empirical interatomic potentials optimized for phonon properties. *npj Comput. Mater.* **3**, 1–7 (2017).
- Dodson, B. W. Development of a many-body Tersoff-type potential for silicon. *Phys. Rev. B* **35**, 2795 (1987).
- Arora, J. S. *Introduction to Optimum Design* (Elsevier, 2004).
- Narayanan, B. et al. Development of a modified embedded atom force field for zirconium nitride using multi-objective evolutionary optimization. *J. Phys. Chem. C* **120**, 17475–17483 (2016).
- Mishra, A. et al. Multiobjective genetic training and uncertainty quantification of reactive force fields. *npj Comput. Mater.* **4**, 1–7 (2018).
- Kandemir, A., Yapicioglu, H., Kinaci, A., Çağın, T. & Sevik, C. Thermal transport properties of MoS₂ and MoSe₂ monolayers. *Nanotechnology* **27**, 055703 (2016).
- Ostadhossein, A. et al. ReaxFF reactive force-field study of molybdenum disulfide (MoS₂). *J. Phys. Chem. Lett.* **8**, 631–640 (2017).
- Jiang, J.-W. Parametrization of Stillinger-Weber potential based on valence force field model: application to single-layer MoS₂ and black phosphorus. *Nanotechnology* **26**, 315706 (2015).
- Lindsay, L. & Broido, D. Optimized Tersoff and Brenner empirical potential parameters for lattice dynamics and phonon thermal transport in carbon nanotubes and graphene. *Phys. Rev. B* **81**, 205441 (2010).
- Jiang, J.-W., Park, H. S. & Rabczuk, T. Molecular dynamics simulations of single-layer molybdenum disulfide (MoS₂): Stillinger-Weber parametrization, mechanical properties, and thermal conductivity. *J. Appl. Phys.* **114**, 064307 (2013).
- Chan, H. et al. Machine learning a bond order potential model to study thermal transport in WSe₂ nanostructures. *Nanoscale* **11**, 10381–10392 (2019).
- Gale, J. D. GULP: A computer program for the symmetry-adapted simulation of solids. *J. Chem. Soc. Faraday Trans.* **93**, 629–637 (1997).
- Deb, K. & Jain, H. An evolutionary many-objective optimization algorithm using reference-point-based nondominated sorting approach, part I: solving problems with box constraints. *IEEE Trans. Evol. Comput.* **18**, 577–601 (2013).
- Buckingham, R. A. The classical equation of state of gaseous helium, neon and argon. *Proc. Math. Phys. Eng. Sci.* **168**, 264–283 (1938).
- Manzeli, S., Ovchinnikov, D., Pasquier, D., Yazyev, O. V. & Kis, A. 2D transition metal dichalcogenides. *Nat. Rev. Mater.* **2**, 17033 (2017).
- Radisavljevic, B., Radenovic, A., Brivio, J., Giacometti, V. & Kis, A. Single-layer MoS₂ transistors. *Nat. Nanotechnol.* **6**, 147–150 (2011).
- Wu, W. et al. Piezophototronic effect in single-atomic-layer MoS₂ for strain-gated flexible optoelectronics. *Adv. Mater.* **28**, 8463–8468 (2016).
- Kumar, K. S., Choudhary, N., Jung, Y. & Thomas, J. Recent advances in two-dimensional nanomaterials for supercapacitor electrode applications. *ACS Energy Lett.* **3**, 482–495 (2018).
- Jariwala, D., Sangwan, V. K., Lauhon, L. J., Marks, T. J. & Hersam, M. C. Emerging device applications for semiconducting two-dimensional transition metal dichalcogenides. *ACS Nano* **8**, 1102–1120 (2014).
- Gu, X. & Zhao, C. Thermal conductivity of single-layer MoS₂(1–x)Se_{2x} alloys from molecular dynamics simulations with a machine-learning-based interatomic potential. *Comput. Mater. Sci.* **165**, 74–81 (2019).
- Apte, A. et al. Structural phase transformation in strained monolayer MoWSe₂ alloy. *ACS Nano* **12**, 3468–3476 (2018).
- Patra, T. K. et al. Defect dynamics in 2-D MoS₂ probed by using machine learning, atomistic simulations, and high-resolution microscopy. *ACS Nano* **12**, 8006–8016 (2018).
- Tadmor, E. B. & Miller, R. E. *Modeling Materials: Continuum, Atomistic and Multi-scale Techniques* (Cambridge University Press, 2011).
- Géron, A. *Hands-on Machine Learning with Scikit-Learn, Keras, and TensorFlow: Concepts, Tools, and Techniques to Build Intelligent Systems* (O'Reilly Media, 2019).
- Duerloo, K.-A. N., Li, Y. & Reed, E. J. Structural phase transitions in two-dimensional Mo- and W-dichalcogenide monolayers. *Nat. Commun.* **5**, 1–9 (2014).
- Lin, Y.-C., Dumcenco, D. O., Huang, Y.-S. & Suenaga, K. Atomic mechanism of the semiconducting-to-metallic phase transition in single-layered MoS₂. *Nat. Nanotechnol.* **9**, 391–396 (2014).
- Ishibuchi, H., Imada, R., Setoguchi, Y. & Nojima, Y. in *2016 IEEE Congress on Evolutionary Computation (CEC)*, 3045–3052 (IEEE, 2016).
- Lin, F.-Y. & MacKerell, A. D. Jr. Polarizable empirical force field for halogen-containing compounds based on the classical Drude oscillator. *J. Chem. Theory Comput.* **14**, 1083–1098 (2018).
- Vanommeslaeghe, K. et al. CHARMM general force field: a force field for drug-like molecules compatible with the CHARMM all-atom additive biological force fields. *J. Comput. Chem.* **31**, 671–690 (2010).
- Henkelman, G., Uberuaga, B. P. & Jónsson, H. A climbing image nudged elastic band method for finding saddle points and minimum energy paths. *J. Chem. Phys.* **113**, 9901–9904 (2000).
- Saxena, D. K., Duro, J. A., Tiwari, A., Deb, K. & Zhang, Q. Objective reduction in many-objective optimization: Linear and nonlinear algorithms. *IEEE Trans. Evol. Comput.* **17**, 77–99 (2012).
- Zhao, X. et al. Mo-terminated edge reconstructions in nanoporous molybdenum disulfide film. *Nano Lett.* **18**, 482–490 (2018).
- Gu, X. & Yang, R. Phonon transport in single-layer transition metal dichalcogenides: a first-principles study. *Appl. Phys. Lett.* **105**, 131903 (2014).
- Zhang, X. et al. Measurement of lateral and interfacial thermal conductivity of single and bilayer MoS₂ and MoSe₂ using refined optothermal Raman technique. *ACS Appl. Mater. Interfaces* **7**, 25923–25929 (2015).
- Croy, A. Bending rigidities and universality of flexural modes in 2D crystals. *J. Phys. Mater.* **3**, 02LT03 (2020).
- Jaramillo-Botero, A., Naserifar, S. & Goddard, W. A. III General multiobjective force field optimization framework, with application to reactive force fields for silicon carbide. *J. Chem. Theory Comput.* **10**, 1426–1439 (2014).
- Betz, R. M. & Walker, R. C. Paramfit: automated optimization of force field parameters for molecular dynamics simulations. *J. Comput. Chem.* **36**, 79–87 (2015).
- Chenoweth, K., Van Duin, A. C. & Goddard, W. A. ReaxFF reactive force field for molecular dynamics simulations of hydrocarbon oxidation. *J. Phys. Chem. A* **112**, 1040–1053 (2008).
- Larentzos, J. P., Rice, B. M., Byrd, E. F., Weingarten, N. S. & Lill, J. V. Parameterizing complex reactive force fields using multiple objective evolutionary strategies (MOES). Part 1: ReaxFF models for cyclotrimethylene trinitramine (RDX) and 1, 1-diamino-2, 2-dinitroethene (FOX-7). *J. Chem. Theory Comput.* **11**, 381–391 (2015).
- Lin, J., Pantelides, S. T. & Zhou, W. Vacancy-induced formation and growth of inversion domains in transition-metal dichalcogenide monolayer. *ACS Nano* **9**, 5189–5197 (2015).
- Soler, J. M. et al. The SIESTA method for ab initio order-N materials simulation. *J. Phys. Condens. Matter* **14**, 2745 (2002).

52. Perdew, J. P., Burke, K. & Ernzerhof, M. Generalized gradient approximation made simple. *Phys. Rev. Lett.* **77**, 3865 (1996).
53. Dunning, T. & Hay, P. *Modern Theoretical Chemistry* (ed. Schaefer H.F.) (Plenum, 1977).
54. Troullier, N. & Martins, J. L. Efficient pseudopotentials for plane-wave calculations. *Phys. Rev. B* **43**, 1993 (1991).
55. Persson, K. Materials data on MoSe₂ (SG: 194) by Materials Project <https://doi.org/10.17188/1191826> (2014).
56. Moreno, J. & Soler, J. M. Optimal meshes for integrals in real-and reciprocal-space unit cells. *Phys. Rev. B* **45**, 13891 (1992).
57. Cooper, R. C. et al. Nonlinear elastic behavior of two-dimensional molybdenum disulfide. *Phys. Rev. B* **87**, 035423 (2013).
58. Plimpton, S. Fast parallel algorithms for short-range molecular dynamics. *J. Comput. Phys.* **117**, 1–19 (1995).
59. Togo, A. & Tanaka, I. First principles phonon calculations in materials science. *Scr. Mater.* **108**, 1–5 (2015).
60. Khan, A. I. et al. Equilibrium molecular dynamics (MD) simulation study of thermal conductivity of graphene nanoribbon: a comparative study on MD potentials. *Electronics* **4**, 1109–1124 (2015).
61. Frenkel, D. & Smit, B. *Understanding Molecular Simulation: from Algorithms to Applications*, Vol. 1 (Elsevier, 2001).
62. Stukowski, A. Visualization and analysis of atomistic simulation data with OVITO—the Open Visualization Tool. *Modell. Simul. Mater. Sci. Eng.* **18**, 015012 (2009).
63. Fortin, F.-A., De Rainville, F.-M., Gardner, M.-A. G., Parizeau, M. & Gagné, C. DEAP: evolutionary algorithms made easy. *J. Mach. Learn. Res.* **13**, 2171–2175 (2012).
64. Hold-Geoffroy, Y., Gagnon, O. & Parizeau, M. In *Proceedings of the 2014 Annual Conference on Extreme Science and Engineering Discovery Environment*, 1–8 (Association for Computing Machinery, 2014).

ACKNOWLEDGEMENTS

The authors acknowledge the support of the National Science Foundation, through award CMMI 1953806, and computational resources provided by the Center of Nanoscale Materials at Argonne National Laboratory, as well as the Quest High Performance Computing Cluster at Northwestern University. Use of the Center for Nanoscale Materials, an Office of Science user facility, was supported by the U.S. Department of Energy, Office of Science, Office of Basic Energy Sciences, under Contract No. DE-AC02-06CH11357. The authors acknowledge Dr. Henry Chan for the helpful discussions and suggestions.

AUTHOR CONTRIBUTIONS

X.Z. developed the optimization protocol, carried out optimization and MD simulations, and analyzed the results. H.N. proposed the multi-objective optimization approach, conducted ab initio calculations, and contributed to the improvement of the protocol. J.T.P. guided the ab initio calculations and contributed to the improvement of the protocol. S.K.R.S.K. and J.L.M.-C. provided valuable comments and suggestions to the work. H.D.E. designed the research, interpreted the results, and directed the project. All authors contributed to the discussions of results and writing of the manuscript. X.Z. and H.N. contributed equally to this work.

COMPETING INTERESTS

The authors declare no competing interests.

ADDITIONAL INFORMATION

Supplementary information The online version contains supplementary material available at <https://doi.org/10.1038/s41524-021-00573-x>.

Correspondence and requests for materials should be addressed to H.D.E.

Reprints and permission information is available at <http://www.nature.com/reprints>

Publisher's note Springer Nature remains neutral with regard to jurisdictional claims in published maps and institutional affiliations.



Open Access This article is licensed under a Creative Commons Attribution 4.0 International License, which permits use, sharing, adaptation, distribution and reproduction in any medium or format, as long as you give appropriate credit to the original author(s) and the source, provide a link to the Creative Commons license, and indicate if changes were made. The images or other third party material in this article are included in the article's Creative Commons license, unless indicated otherwise in a credit line to the material. If material is not included in the article's Creative Commons license and your intended use is not permitted by statutory regulation or exceeds the permitted use, you will need to obtain permission directly from the copyright holder. To view a copy of this license, visit <http://creativecommons.org/licenses/by/4.0/>.

© The Author(s) 2021